Plasma-based microwave power limitation in a printed transmission line

Lucas Fuster, Gerjan Hagelaar, Romain Pascaud, Antoine Simon, Patrick Hoffmann, Laurent Liard, Olivier Pascal, Thierry Callegari

To cite this version:

Lucas Fuster, Gerjan Hagelaar, Romain Pascaud, Antoine Simon, Patrick Hoffmann, et al.. Plasma-based microwave power limitation in a printed transmission line: a self-consistent model compared with experimental data. Plasma Sources Science and Technology, 2022, 31 (2), pp.025009. 10.1088/1361-6595/ac4848 . hal-03759205

HAL Id: hal-03759205
https://hal.science/hal-03759205

Submitted on 23 Aug 2022

Plasma-based microwave power limitation in a printed transmission line: a self-consistent model compared with experimental data

Lucas Fuster[1,2,3], **Gerjan Hagelaar**[2], **Romain Pascaud**[3], **Antoine Simon**[4], **Patrick Hoffmann**[1], **Laurent Liard**[2], **Olivier Pascal**[2] **and Thierry Callegari**[2]

[1]Commissariat à l'Energie Atomique et aux Energies Alternatives – Centre de Gramat, BP 80200 46500 Gramat – France
[2]LAPLACE, Université de Toulouse, CNRS, INPT, UPS, Toulouse, France
[3]ISAE-SUPAERO, Université de Toulouse, France
[4]ANYWAVES, Toulouse, France

E-mail: `lucas.fuster@laplace.univ-tlse.fr`

August 2021

Abstract. Plasma-based microwave power limitation in a suspended microstrip transmission line integrating a micro hollow cathode discharge (MHCD) in its center is experimentally and numerically studied. Transient and steady state microwave power measurements exhibit a limitation threshold of 28 dBm and time responses of 25 microseconds. Intensified charge-coupled device (ICCD) imaging shows that microwave breakdown occurs at the top of the MHCD. The plasma then extends towards the microwave source within the suspended microstrip transmission line. Besides, a self-consistent model is proposed to simulate the non-linear interaction between microwave and plasma. It gives numerical results in agreement with the measurements, and show that the plasma expansion during the transient response is related to a shift between the ionization source term and the electron density maximum. The propagation speed, under the tested conditions, depends mainly on the stepwise ionization from the excited states.

Submitted to: *Plasma Sources Sci. Technol.*

1. Introduction

With the development of high-power microwave (HPM) sources [1], the susceptibility of microwave receivers becomes an important issue [2]. As a result, microwave power limiters are sometimes introduced in receivers before sensitive components to avoid permanent damage [3]. A good microwave power limiter should have low insertion loss below a given input power threshold so as not to increase the noise figure of the receiver, and above this limiting threshold it should quickly reduce its output power, known as leakage power, below a safe value.

Microelectromechanical systems (MEMS) [4], high-temperature superconductors [5, 6], or phase-transition materials [7] have been used as active elements for microwave power limitation, but most current solutions use solid-state components such as positive-intrinsic-negative (PIN) diodes [8–10]. PIN diodes generally have modest insertion loss and fast response times while offering small dimensions, relatively simple implementation, and low cost. However, their power handling may not be sufficient with regard to the HPM sources currently under development [11].

Because of their high power handling capability, plasma-based microwave power limiters are also investigated [12–22]. For such limiters, the incident HPM signal causes gas breakdown, and this microwave-driven plasma discharge then absorbs and/or reflects the incoming power, thus limiting the output power. Plasma-based limiters were first implemented in waveguide technology in transmit-receive (TR) tubes, which are still used in duplexers for high-power pulsed radar systems [12]. However, with dimensions of the order of several centimeters, TR tubes remain bulky and not suitable for integration on printed circuit boards, the most widespread technology for the design of microwave receivers.

As far as we know, Patel *et al.* designed the first plasma-based microwave power limiter in planar printed circuit technology, but its high limiting threshold of 47 dBm clearly restricted its use [13]. Since then, this limiting threshold has been successfully reduced and/or controlled using resonant circuits [14], pre-ionization techniques [20], or both [15, 18]. In resonant circuits, the magnitude of the electric field is enhanced at resonance, thus reducing the microwave power required for gas breakdown [14, 18]. Regarding pre-ionization, it provides seed electrons such that the breakdown electric field drastically decreases [20, 23]. It is interesting to note that similar solutions have also been implemented in two-dimensional (2D) photonic crystals (PhC) which are investigated for the realization of millimeter-wave receivers [17, 19, 21].

Although these plasma-based limiters have interesting performances, most of current work is based on experimental studies and few on numerical models that may provide interesting information on the interaction between microwave power and plasma discharge. For instance, numerical diagnostics of the electron density have been proposed [16,17,21]. In that case, the plasma is modelled as a uniform three-dimensional (3D) object described by the Drude model in an electromagnetic software, and its electron density is sought in simulation in order to obtain the same response as in measurement. Recently, Gregório *et al.* have proposed to couple fluid and Maxwell equations to study the interaction between microwave and plasma [24]. This model was applied to the simulation of a PhC power limiter, but no comparison with measurements was provided. Finally, the lack of validated models that faithfully reproduce the non-linear interaction within plasma-based microwave power limiters makes their design and optimization difficult.

In this paper, we present the design of a plasma-based microwave power limiter in suspended microstrip technology. In addition to having good performance as a limiter, its geometry allows it to be studied with a self-consistent 2D numerical model. A direct comparison between experimental and numerical results shows that this model is predictive and that it can be used for studying the proposed limiter.

2. Device under test and experimental setup

2.1. Device under test

The exploded view of the proposed plasma-based microwave power limiter is shown in figure 1b. It is similar to the one studied by Simon *et al.* in [20], but the microstrip transmission line has been replaced by a suspended microstrip transmission line as described below.

The microwave power limiter in suspended microstrip technology, also called device under test (DUT) hereafter, is made up of several planar layers stacked on top of each other. As shown in figure 1b, the suspended microstrip line consists of two conductors, namely a ground plane and a line printed on a thin dielectric substrate. Dielectric spacers are placed on both ends of the transmission line to provide a constant gap between the two conductors, and thus form a low pressure gas-filled cavity that hosts the plasma discharge during the microwave power limitation. Note that the cavity remains open on its sides to allow optical measurements of the plasma during the experiments. Due to the dielectric spacers, the input and output of the whole transmission line are similar to microstrip transmission lines, whereas the middle part is a suspended one. The dielectric substrates are Rogers RO4003C with $\varepsilon_r = 3.55$ and $\tan\delta = 0.0021$. The thickness of the dielectric spacers

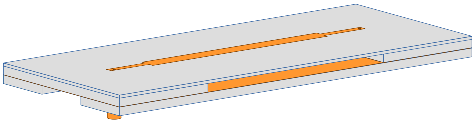

(a) General view.

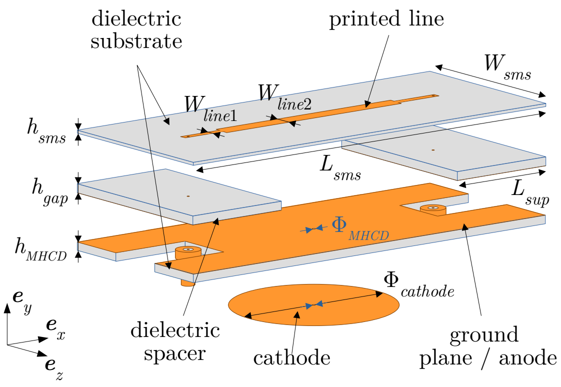

(b) Exploded view.

Figure 1. Schematic of the plasma-based microwave power limiter in suspended microstrip technology.

is $h_{gap} = 1.524$ mm, their length is $L_{sup} = 50$ mm, and the thickness of the suspended dielectric substrate is $h_{sms} = 0.508$ mm. The width of the printed line varies according to the dielectric configuration between the conductors in order to achieve a 50 Ω characteristic impedance along the whole transmission line, and thus allows the impedance matching of the DUT. Therefore, we have $W_{line1} = 4.5$ mm for the microstrip transmission line section and $W_{line2} = 8$ mm for the suspended one. Finally, the microwave part of the DUT is $W_{sms} = 100$ mm wide, $L_{sms} = 200$ mm long, and $h_{tot} = h_{gap} + h_{sms} = 2.032$ mm thick, whereas the cavity is 100 mm long. Note that the transmission line is connected at both ends to 50 Ω coaxial straight connectors.

The principle of operation of this plasma-based microwave power limiter has already been exposed in [15, 20], and it is here briefly recalled. When a microwave signal is propagating along the transmission line, namely along x direction, the electric field is mostly confined between the ground plane and suspended microstrip and oriented along y direction. If the incoming microwave power is large enough, for instance during an HPM attack, gas breakdown may be ignited in the low pressure gas-filled cavity. This microwave-driven plasma then absorbs and/or reflects the HPM signal thereby reducing the output power. In order to reduce the microwave power limiting threshold, pre-ionization is used [20, 21, 23]. It consists in generating seed electrons inside the cavity with a DC micro-hollow cathode discharge (MHCD) [25].

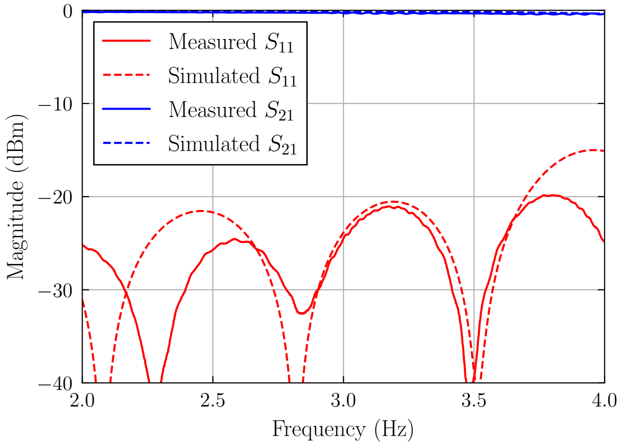

Figure 2. Simulated and measured small-signal reflection (S_{11}) and transmission (S_{21}) coefficients of the suspended microstrip line without pre-ionization as a function of the frequency.

The DC circuit for pre-ionization, that is to say the MHCD, uses a cylindrical copper cathode printed on a Rogers RO4003C dielectric substrate below the ground plane. Its diameter is $\Phi_{cathode} = 80$ mm. As observed in figure 1b, the ground plane of the transmission line is used as the anode for the MHCD. A cylindrical hole is drilled in the center of the cathode through the dielectric substrate and the two electrodes. The dimensions of the MHCD hole have been chosen to $h_{MHCD} = 1.524$ mm and $\Phi_{MHCD} = 1$ mm to lower the breakdown voltage at 10 Torr in Argon. The MHCD is thus in normal glow regime with DC current $I_{DC} = 3$ mA [26].

The DUT was measured with a vector network analyzer (Rohde & Schwarz, ZVL13) and simulated using Ansys HFSS, a 3D frequency-domain electromagnetic solver. Figure 2 presents the magnitude of the small-signal reflection and transmission coefficients (i.e., S_{11} and S_{21} parameters, respectively) of the DUT without pre-ionization. A good agreement is observed with a measured reflection coefficient lower than −20 dB and transmission coefficient better than −0.4 dB for the bandwidth of the experimental setup, namely 2 to 4 GHz.

2.2. *Experimental setup*

Figure 3 shows the experimental setup. The DUT is placed in a quartz vacuum chamber evacuated to a base pressure of 10^{-5} Torr by a vacuum pump station (Edwards Vacuum, TSM1D1001) and then backfilled with Argon to the desired pressure, namely 10 Torr, which is measured by a piezo transducer gauge (Pfeiffer Vacuum, CMR361). The Argon flow

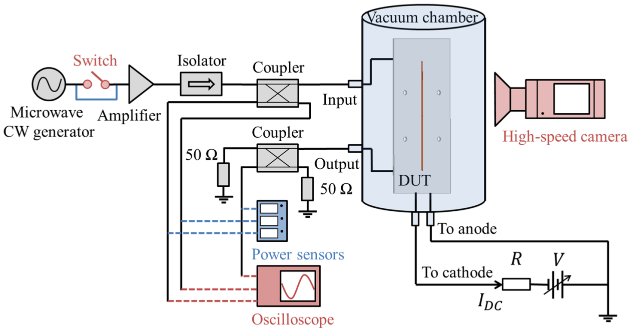

Figure 3. Experimental setup for steady-state (blue configuration) and transient (red configuration) high-power microwave measurements.

is fixed to 0.1 L/min using a mass flow controller (Bronkhorst, EL-FLOW Prestige). The DUT is thus totally immersed in a large volume of Argon, including the cavity between the ground plane and the suspended microstrip line. A high voltage generator (Technix, SR2KV-2KW) is connected to the MHCD electrodes through a DC vacuum feedthrough. It is used to ignite and sustain the DC plasma discharge for pre-ionization. The current I_{DC} flowing through the discharge is limited by a series resistor $R = 10\ k\Omega$. Regarding the high-power microwave measurement devices, they allow for both steady-state and transient measurements.

The steady-state measurement setup involves the blue and black components in figure 3. A continuous wave (CW) microwave signal is generated by a microwave generator (Anapico, APSIN20G) and then amplified by a power amplifier (MC2 Technologies, HPA60W2-4G). This power amplifier (PA) has a maximum output power of 60 W between 2 and 4 GHz. The HPM signal is then delivered to the DUT through 50 Ω coaxial vacuum feedthroughs. An isolator (Quest Microwave, NM2040C02) has been inserted between the PA and the first coupler in order to protect the microwave amplifier against high reflected power. Finally, leakage power of the DUT is dissipated by a high-power 50 Ω termination (Weinschel Associates, WA1448). As shown in figure 3, the input, reflected, and output powers of the DUT are coupled by means of two -30 dB directional couplers (SHX, DDTO-3-30). One is connected between the PA and the input port of the DUT while the other is connected between its output and the 50 Ω termination. Power measurements are done thanks to three power sensors (Keysight, U8481A) connected to the coupled ports of the two couplers. Insertion loss from coaxial cables, feedthroughs, and couplers have been measured with a vector network analyzer (Rohde & Schwarz ZVL13). All steady-state power measurements reported thereafter have thus been corrected so that they refer to DUT ports. Note that the frequency range is limited to $2-4$ GHz due to the PA, isolator, and couplers characteristics, and the maximum power at the DUT input is 45 dBm because of coaxial feedthroughs power handling.

For transient measurements, slight modifications are done to the experimental setup (red and black components in figure 3). A microwave switch (American Microwave Corporation, SWMDJV- 1DT-2ATT) is first inserted between the microwave signal generator and the PA. The resulting signal is a high-power microwave pulse. In addition to that, the power sensors are replaced by an oscilloscope (Keysight, MSO9254A) that records the input, reflected, and output signals of the DUT. Finally, a camera (Princeton Instruments, PI-MAX 512) with a red-blue optimized intensifier (Princeton Instruments, GEN II) is added to the experimental setup in side view of the DUT. The microwave switch, the oscilloscope, and the camera are synchronized with a control signal whose pulse width and repetition frequency are equal to 1 ms and 100 Hz, respectively. Each picture results from a 200 ms exposure time with a 20 ns gate time.

3. Model and numerical setup

In order to study the non-linear response of the plasma-based microwave power limiter described in figure 1, a 2D self-consistent numerical model was implemented. This model has already been detailed in [27], but we remind here its principles and point out the specific adaptations we made for the present study.

As the plasma density and chemistry evolve on a long time scale (microsecond) compared to that of the microwave oscillations (sub-nanosecond), our model is composed of two sub-models describing these two time scales separately. Both sub-models are based on a combination of fluid equations and Maxwell equations. The sub-model for the plasma evolution is obtained by averaging these equations over the short (microwave) time scale, while that for the microwaves neglects the time variations of the plasma parameters. The sub-models are coupled via the absorbed microwave power (activating the plasma), and the electron density and collision frequency (affecting the microwaves). Thus, during the simulation of the plasma evolution, the microwave model is periodically called to update the microwave power absorption profile, using the latest plasma profile.

In the following sections, we first describe the model geometry, then the two sub-models, and finally the plasma-chemical processes that are taken into account.

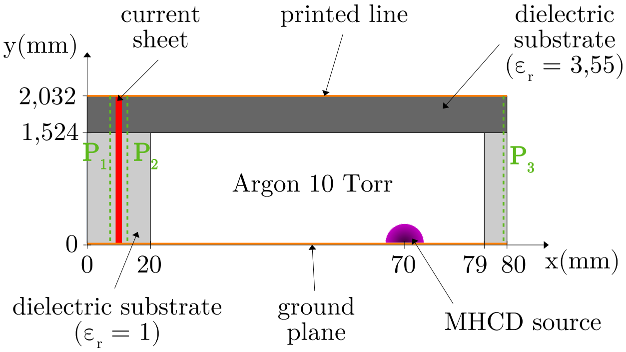

Figure 4. Model geometry of the suspended microstrip circuit. Metal parts are in orange and dielectric parts in grey.

3.1. Simulated geometry

The suspended microstrip transmission line shown in figure 1 has a large width-to-height ratio $w_{line2}/(h_{gap}+h_{sms})$ of 3.9. As a result, fringing effects can be neglected and the central longitudinal part of the DUT can be seen as an inhomogeneously dielectric filled parallel-plate transmission line [28]. We thus propose to simulate it using the 2D simulation domain described in figure 4 that represents a part in the (x, y) plane of the suspended microstrip transmission line.

This 2D model assumes that the geometry is invariant in the z direction, and that plasma and microwave characteristics are uniform along z, but still functions of x and y. Since the dominant mode is the TM$_x$ mode, E_x, E_y, and B_z field components are considered. Note that this mode behaves as a quasi-TEM mode in the low frequency limit, without plasma, and that no higher order modes are excited as long as $k_0(h_{gap} + h_{sms}) \ll 1$, with k_0 the wave number in vacuum [28]. This condition is satisfied at 3 GHz, our frequency of interest.

In order to reduce the computation time, the length of the plasma cavity region to the right of the MHCD source ($x > 70$ mm in figure 4) has been shortened to 9 mm. We verified that it does not modify the numerical results for our microwave power range. The dielectric constant of the two dielectric spacers at the edges of the device has been set equal to 1 in the simulations, instead of 3.55 in the experiment. This modification allows us to reproduce the impedance matching (when there is no plasma in the cavity) that is experimentally obtained by changing the width of the printed line of the DUT.

Finally, as shown in figure 4, the microwave field is excited by an artificial current sheet near the left edge of the simulation domain as explained in section 3.2. Regarding the MHCD, it is not simulated in detail but modelled by adding a localized source term in plasma equations which reproduces a realistic electron density and ensures that the gas breakdown occurs at the same incident power as in experiments. This MHCD source term has a Gaussian profile centered at $x = 70$ mm in figure 4, near the ground plane, with a width of 1 mm in the x direction, and a width of 0.3 mm in the y direction. The amplitude of the source term is of 1.35×10^{23} m^{-3}.s^{-1}.

3.2. Microwave model

The microwaves are described by solving the Maxwell equations [27]:

$$\nabla \times \tilde{\boldsymbol{E}} = -\frac{\partial \tilde{\boldsymbol{B}}}{\partial t} \tag{1}$$

$$\frac{1}{\mu_0} \nabla \times \tilde{\boldsymbol{B}} = \tilde{\boldsymbol{J}}_{exc} - e n_e \tilde{\boldsymbol{v}}_e + \varepsilon_0 \varepsilon_r \frac{\partial \tilde{\boldsymbol{E}}}{\partial t} \tag{2}$$

where $\tilde{\boldsymbol{E}}$ and $\tilde{\boldsymbol{B}}$ are the oscillating electric and magnetic fields, n_e the electron density obtained from the plasma model, $\tilde{\boldsymbol{v}}_e$ the oscillating component of the electron mean velocity, $\tilde{\boldsymbol{J}}_{exc}$ an external oscillating current which excites the microwaves and μ_0 is the magnetic permeability of vacuum. The second term on the right hand side of equation (2) is an approximation of the plasma current density, neglecting the ion contribution (because $m_i \gg m_e$) and oscillations of the electron density ($\tilde{n}_e \ll n_e$).

The oscillating electron velocity is obtained from the local momentum equation

$$\frac{\partial \tilde{\boldsymbol{v}}_e}{\partial t} = -\frac{e}{m_e} \tilde{\boldsymbol{E}} - \nu_e \tilde{\boldsymbol{v}}_e, \tag{3}$$

where ν_e is the momentum transfer frequency of collisions with the gas. This set of equations is solved by the finite-difference time-domain (FDTD) method, using a Yee mesh that coincides with the mesh of the plasma model, with perfect conductor boundary conditions at the metal boundaries (top and bottom) and first-order Mur absorption boundary conditions at the open boundaries (left and right) [29].

For the excitation current $\tilde{\boldsymbol{J}}_{exc}$ in equation (2) we use a thin current sheet near the left edge of the simulation domain (see figure 4). This generates an electric field in the y direction which then propagates both to the right and to the left, while inducing other field components and interfering with the wave reflected by the plasma. We fix the amplitude of $\tilde{\boldsymbol{J}}_{exc}$ at an arbitrary value, hence the amplitudes of $\tilde{\boldsymbol{E}}$, $\tilde{\boldsymbol{B}}$, and $\tilde{\boldsymbol{v}}_e$ are also arbitrary and need to be normalized afterwards. This is done by imposing a fixed incident power, as follows.

First the amplitude of the reflected wave is determined by combining the net fields in two planes P$_1$ and P$_2$ located at a small distance δ to the left

#	Reaction	Reaction rate	Comment	Ref.
1	$e + Ar \mapsto 2e + Ar^+$	EEDF ($\mathrm{m^3.s^{-1}}$)	Direct ionization	[30]
$2, 3$	$e + Ar \mapsto e + Ar^*_{m,r}$	EEDF ($\mathrm{m^3.s^{-1}}$)	Impact excitation	[30]
$4, 5$	$e + Ar^*_{m,r} \mapsto e + Ar$	EEDF ($\mathrm{m^3.s^{-1}}$)	De-excitation	[30]
$6, 7$	$e + Ar^*_{m,r} \mapsto 2e + Ar^+$	EEDF ($\mathrm{m^3.s^{-1}}$)	Two-step ionization	[31–33]
$8, 9$	$e + Ar^*_m \rightleftharpoons e + Ar^*_r$	EEDF ($\mathrm{m^3.s^{-1}}$)	Metastable quenching	[34]
10	$Ar^*_r \mapsto Ar + h\nu$	$5.85 \times 10^5\ \mathrm{s^{-1}}$	Radiative de-excitation	[35–37]
$11, 12, 13$	$Ar^*_{m,r} + Ar^*_{m,r} \mapsto e + Ar_2^+$	$0.7 \times 6.4 \times 10^{-16}\ \mathrm{m^3.s^{-1}}$	Ar^* pooling ionization	[38]
$14, 15, 16$	$Ar^*_{m,r} + Ar^*_{m,r} \mapsto e + Ar + Ar^+$	$0.3 \times 6.4 \times 10^{-16}\ \mathrm{m^3.s^{-1}}$	Ar^* pooling ionization	[38]
17	$Ar^+ + 2Ar \mapsto Ar_2^+ + Ar$	$2.5 \times 10^{-43}\ \mathrm{m^6.s^{-1}}$	Molecular ion formation	[39]
18	$e + Ar_2^+ \mapsto Ar + Ar^*_m$	$7.35 \times 10^{-14} \times T_e^{-2/3}\ \mathrm{m^3.s^{-1}}$	Dissociative recombination	[40]

Table 1. Complete set of reactions taken into account in the numerical model.

and to the right of the current sheet, respectively (see figure 4)

$$E^2_{refl} = \frac{1}{2\sin^2(\beta\delta)} \left\langle (\tilde{E}_{y,2} - \tilde{E}_{y,1})^2 \right\rangle_t \tag{4}$$

$$B^2_{refl} = \frac{1}{2\cos^2(\beta\delta)} \left\langle (\tilde{B}_{z,1} + \tilde{B}_{z,2})^2 \right\rangle_t \tag{5}$$

where the angle brackets $\langle . \rangle_t$ indicate the time-average over the microwave period and β is the propagation phase constant of the dominant mode within this transmission line, given in the low frequency limit by [28]

$$\beta \approx k_0 \sqrt{\frac{h_{gap} + h_{sms}}{h_{gap} + h_{sms}/\varepsilon_r}} \tag{6}$$

that is to say $\beta \approx 1.1 k_0$ for our problem.

The time-averaged reflected power is then found by integrating the reflected Poynting vector over the cross section of the transmission line

$$P_{refl} = \frac{\alpha L_z}{2\mu_0} \int E_{refl} B_{refl}\, \mathrm{d}y \tag{7}$$

where L_z is the effective size of the model geometry in the z direction ($\approx$ width of the transmission line) and α is a normalization factor to correct for the arbitrary amplitude of the excitation current. Finally, subtracting (7) from the net power passing through the plane $\mathrm{P_2}$, we get an expression for the incident power which allows us to determine the normalization factor α

$$\frac{1}{\alpha} = \frac{L_z}{\mu_0 P_{in}} \int \left(\langle \tilde{E}_{y,2} \tilde{B}_{z,2} \rangle_t \ - \frac{1}{2} E_{refl} B_{refl} \right) \mathrm{d}y, \tag{8}$$

where P_{in} is a constant incident power, one of the main input parameters of our simulations.

Once the normalization factor is known, the microwave power absorbed by the plasma follows from

$$P_{abs} = L_z \int\int P_e(x,y) n_e(x,y) \mathrm{d}x\mathrm{d}y \tag{9}$$

where the integrals are over the plasma region and

$$P_e = \alpha \left\langle -e\tilde{\boldsymbol{E}} \cdot \tilde{\boldsymbol{v}}_e \right\rangle_t \tag{10}$$

is the time-averaged absorbed power per electron, which is injected into the energy equation (**??**) of the plasma model. In addition, the transmitted power P_{out} is calculated by integrating the Poynting vector over the plane $\mathrm{P_3}$ at the right domain edge. Our simulations accurately reproduce steady-state energy conservation $P_{in} = P_{refl} + P_{abs} + P_{out}$.

For optimal consistency, we calibrated the value of L_z using full 3D simulations of the DUT without plasma with Ansys HFSS. From these simulations we determined the magnitude of the electric field $\tilde{E}_{3D}$ at the position of the MHCD as a function of the input power P_{3D}, and then adjusted L_z such as to reproduce these results

$$\frac{\mu_0 \langle \tilde{E}^2 \rangle_t}{L_z \int \langle \tilde{E}_y \tilde{B}_z \rangle_t \mathrm{d}y} = \frac{\langle \tilde{E}^2_{3D} \rangle_t}{P_{3D}}. \tag{11}$$

From this calibration, we found a value of $L_z = 7.34$ mm, which we then fixed in the simulations. (The geometrical value is 8 mm, similar but a little different.)

3.3. Chemical model

The electrons e and five different Argon species are considered in our simulations: atomic ions Ar^+, molecular ions Ar_2^+, two excited species Ar^*_m and Ar^*_r, and background gas Ar. The complete set of chemical reactions between these species is presented in Table 1.

The rate coefficients of reactions 1 to 9 were calculated from cross section data with the BOLSIG+ software [41], which solves the electron Boltzmann equation in order to take into account the shape of the electron energy distribution function (EEDF) self-consistently. These rate coefficients are used in the form of lookup tables as a function of T_e, assumed to be equal to 2/3 times the electron mean energy.

The excited Argon states are grouped into two species: an effective metastable species Ar^*_m and an effective resonant species Ar^*_r. These species are assumed to consist mainly of the first four excited

Argon states, namely the $1s_5$ and $1s_3$ metastable states and the $1s_4$ and $1s_2$ resonant states (in Paschen notation), respectively. However, the rate coefficients for the production of these species (reactions 2 and 3) take into account not only direct excitation of the $1s$ states but also cascading from higher states, using the effective excitation cross sections of the Morgan database [30].

The rate coefficients for stepwise ionization (reactions 6 and 7) are based on cross sections for each of the $1s$ states, calculated using the analytical solution proposed by Deutsch *et al.* [31, 32] which is consistent with experimental measurements in Argon [33].

The rate coefficients of reactions 8 and 9 were calculated from cross sections for electron-impact state-to-state transitions between the different $1s$ states taken from the detailed BSR database [34].

The radiative decay rate of A_r^* (reaction 10) was estimated as the average of the natural decay rates of the $1s_4$ and $1s_2$ states, approximately 3.32×10^8 s^{-1} [37], multiplied by an escape factor to account for the effect of resonance radiation imprisonment. For an infinite slab geometry and line broadening due to collisions, the effective escape factor is (see equations (5.17) in [35] and (6.5) in [36])

$$g_{eff} = \frac{1.150}{\pi}\sqrt{\frac{\lambda_{eff}}{3h_{gap}}} \tag{12}$$

where $\lambda_{eff} = 105.8$ nm is the average wavelength of the resonance radiation.

4. Results and discussion

As mentioned previously, both simulations and measurements of the DUT were carried out considering Argon at 10 Torr. In addition, a frequency of 3 GHz was chosen for the HPM signal. All the following results were obtained for these conditions. Unless otherwise stated, the MHCD is always switched on with a DC current I_{DC} equal to 3 mA.

4.1. *Transient results*

4.1.1. *Plasma dynamics and power ratios evolution*

The DUT was first measured using the experimental setup of figure 3 in transient configuration. Optical measurements were achieved with the fast camera to observe the dynamics of the plasma. Both simulation and measurements were conducted using a 40 dBm HPM pulse. The time $t = 0$ μs subsequently refers to the start of the HPM pulse. Note that unlike our experimental setup, the simulation gives us access to the electron density of the plasma as a function of time.

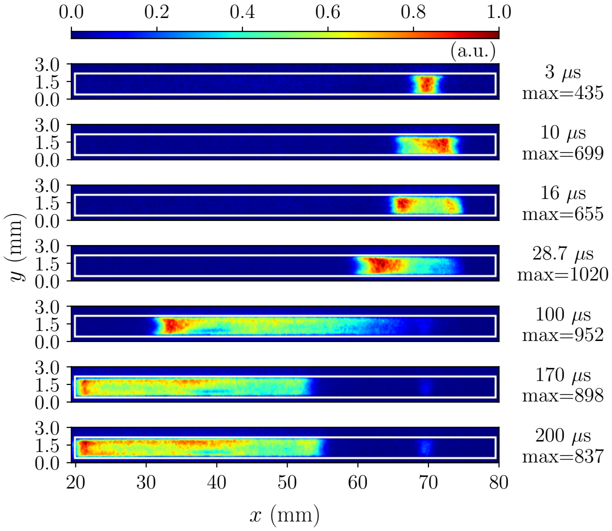

(a) Optical measurements.

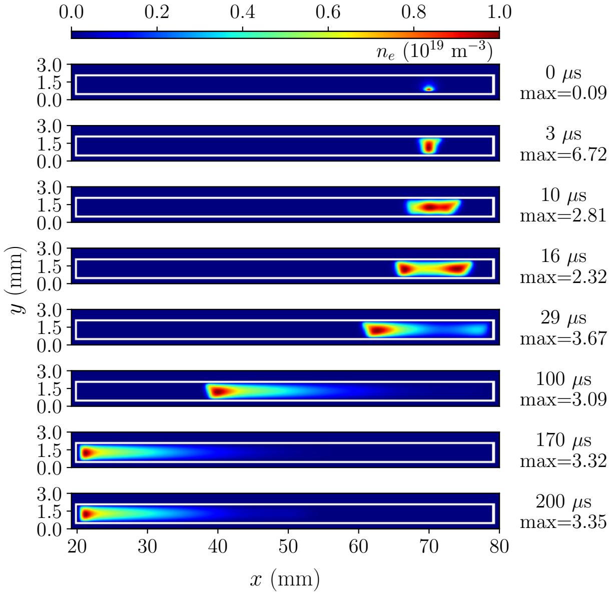

(b) Simulated electron density.

Figure 5. Comparison of simulated and experimental plasma dynamics at different times with $P_{in} = 40$ dBm at 3 GHz and Argon at 10 Torr.

In figure 5, we can see for instance the measured light emitted by the plasma as well as the simulated electron density taken at different times. When microwave gas breakdown occurs in the device, the plasma grows and then moves towards the left, from the position of the MHCD toward the input of the DUT. For an input power $P_{in} = 40$ dBm, the maximum value of the simulated electron density is about 10^{19} m^{-3}.

In addition to that, we measured the instantaneous reflected and output powers, denoted as P_{refl} and P_{out}, respectively. Experimentally, the absorbed power is computed as $P_{abs} = P_{in} - P_{out} - P_{refl}$. Formally, this is the definition of the dissipated power,

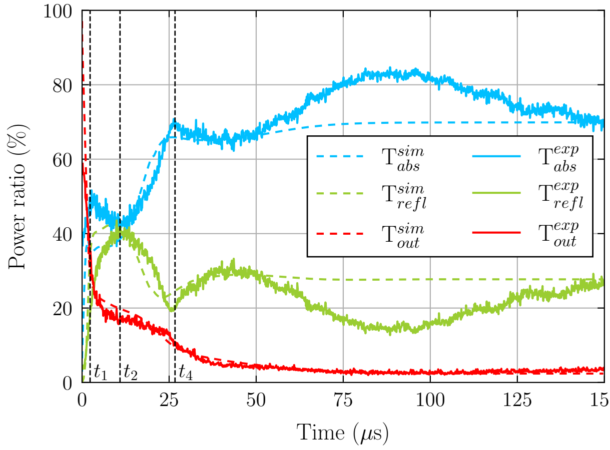

Figure 6. Simulated and measured transient power ratios as a function of time with $P_{in} = 40$ dBm at 3 GHz and Argon at 10 Torr and $I_{DC} = 3$ mA.

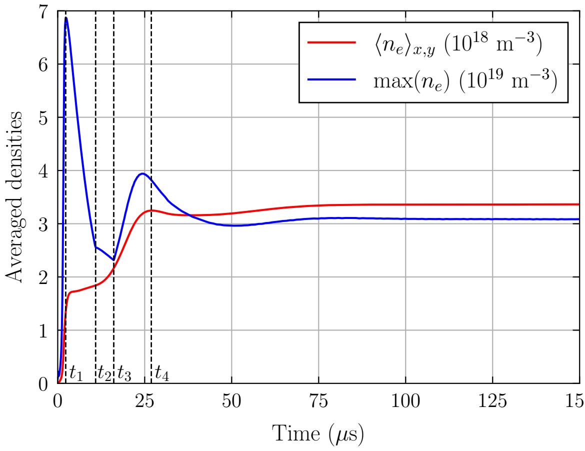

Figure 7. Simulated average electron density as a function of time with $P_{in} = 40$ dBm at 3 GHz and Argon at 10 Torr.

but here, the radiated power from the transmission line remains low and the dissipated power can reasonably be considered as mainly absorbed by the plasma discharge. The simulated reflected, absorbed and output powers have also been measured. From these power results, we can compute the reflected, output, and absorbed power ratios relative to the input power that are denoted T_{refl}, T_{out}, and T_{abs}, respectively.

Figure 6 shows the time evolution of the different power ratios during microwave breakdown with a good agreement between simulation and measurements, even if a discrepancy of 10%, that remains to be understood, appears around 100 μs. We observe the typical response of a mainly absorbing microwave power limiter with its output power ratio that is decreasing over time up to its leakage value while its dissipated power ratio is highly increasing. The power of the HPM signal at the output of the DUT is here reduced by 90 % after 25 μs. Beyond 150 μs, the power ratios no longer change.

The time evolution of the power ratios may be linked to the plasma dynamics. Therefore, in addition to the images of figure 5, figure 7 shows the time evolution of the average electron density over the plasma domain $\langle n_e \rangle_{x,y}$ as well as the maximum of the electron density $max(n_e)$. One can distinguish four steps in the plasma dynamics (the times given are those of the simulation):

(1) Before the beginning of the HPM pulse, the MHCD is in steady-state and it produces a localized electron density of up to 9×10^{17} m^{-3}. From $t = 0$ μs to $t_1 = 2.31$ μs, there is the microwave breakdown with an increasing electron density that reaches a maximum at t_1 (see figure 7). This corresponds to the strong increase of the absorbed power ratio that reaches a local maximum at t_1. As shown in figure 5, this maximum of electron density at this stage remains at the location of the MHCD, that is to say of the pre-ionization region until $t_2 = 10.9$ μs, and the absorbed power ratio remains approximately constant.

(2) From t_2 to $t_3 = 16.11$ μs, the maximum of electron density propagates on the right hand side of the MHCD and starts to decrease. Simultaneously, we observe an increase of the electron density on the left hand side. At t_3, the two peaks of electron density have the same amplitude as shown in figure 5.

(3) From t_3 to $t_4 = 26.70$ μs the electron density finishes to decrease on the right hand side and to increase on the left hand side of the MHCD location. The absorbed power ratio thus increases and the reflection and transmission coefficients both decrease. At t_4 the mean electron density over the plasma domain $\langle n_e \rangle_{x,y}$ reaches its constant value, as shown in figure 7.

(4) Finally, as shown in figure 5, this pattern propagates from the location of the MHCD towards the input of the DUT and a steady-state is reached.

4.1.2. Propagation mechanisms

In this section, we propose to give a more precise description of the physical mechanisms involved in the propagation of the pattern. The numerical code allows us to look at the relative importance of each reaction in the production of electrons. With the reaction rates obtained with the EEDF self-calculated by BOLSIG+ in the local field approximation, no electrons are

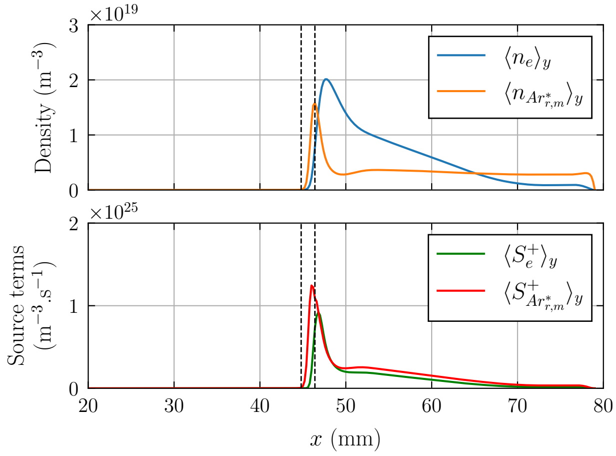

Figure 8. Simulated density profiles and source terms as a function of the position x at $t = 75.2$ μs, for $P_{in} = 40$ dBm. The densities and source terms of metastables and resonant states have been summed as well as the two stepwise ionization source terms of electrons.

created by the direct ionization while 61.1 % and 33.2 % are produced by the ionisation of metastable and resonant states, respectively. These values have been obtained by integration over the plasma domain. In figure 8, we present the electron density profile, the excited states density profile and the source terms of the electrons and the excited states due to the excitation and the stepwise ionisation, defined as:

$$S^+_{Ar^*_{m,r}} = (k_2 + k_3) n_{Ar} n_e \tag{13}$$

$$S^+_e = (k_6 n_{Ar^*_m} + k_7 n_{Ar^*_r}) n_e \tag{14}$$

where k_2, k_3, k_6 and k_7 are the rates of reaction 2, 3, 6 and 7 (see table 1). All the profiles have been averaged over the plasma domain along the y direction. They have been computed at $P_{in} = 40$ dBm and $t = 75.2$ μs. The excited states appear in the first half of the electron density profile, because of the absorption of the electromagnetic energy by the electrons. The source term for the electrons $\langle S^+_e \rangle_y$ reaches a maximum at $x = 46.8$ mm, whereas the electron density profile $\langle n_e \rangle_y$ reaches a maximum at $x = 47.8$ mm. It is this gap between the position of the maxima of $\langle n_e \rangle_y$ and $\langle S^+_e \rangle_y$ that induces the pattern movement. Note that the plasma does not propagate by transport of ions and electrons, but rather by an ionization wave that propagates along the cavity. For input powers between 29 dBm and 42 dBm, the front velocities have been extracted both numerically and experimentally and are presented in figure 9.

The mechanism of the pattern propagation may also be described analytically. According to [42], a fixed point stability analysis for the following nonlinear diffusion equation:

$$\frac{\partial n}{\partial t} - D \frac{\partial^2 n}{\partial x^2} = \nu_i n - r_{ei} n^2 \tag{15}$$

with D the diffusion coefficient, ν_i the ionisation frequency, and r_{ei} the recombination coefficient, all of them being uniform, allows to conclude that the plasma front propagates with a velocity of the order of $v \sim 2\sqrt{D\nu_i}$. Boeuf *et al.* have shown that the diffusion coefficient is of the form [43]:

$$D_{eff} \approx \frac{\alpha}{\alpha + 1} D_e + \frac{1}{\alpha + 1} D_a \tag{16}$$

with D_e and D_a the free and ambipolar diffusion coefficients respectively. The α coefficient controls the cross-over from ambipolar diffusion in the plasma front to free diffusion upstream from the front. It is defined by $\alpha = \nu_i \tau_M$, with ν_i the ionization frequency and $\tau_M = \varepsilon_0 / [e n_e (\mu_e + \mu_i)]$ the Maxwell relaxation time.

We checked that propagation speed from this theory is consistent with that observed in the simulations. In order to do this, we needed to average the theoretical propagation speed over the width of the front region because both D_{eff} and ν_i depend strongly on position in the simulations. We defined the beginning of the front as the point x_i for which the ambipolar diffusion becomes dominant, that is to say for which $\langle \alpha \rangle_y$ becomes inferior to 1%. The end of the plasma front is therefore located at the position x_f for which the ionisation frequency reaches his maximum. The limits of the front are represented by the dashed lines in figure 8. The theoretical front velocity v_f is finally defined as :

$$v_f = \frac{1}{x_f - x_i} \int_{x_i}^{x_f} \mathrm{d}x \, \langle v(x, y) \rangle_y \tag{17}$$

with $v(x, y) = 2\sqrt{D_{eff}(x, y) \nu_i(x, y)}$. The total ionisation frequency ν_i is the sum of the three ionization frequencies ν_1, ν_6, and ν_7 of reactions 1, 6, and 7, respectively. Equation (17) gives a good approximation for the simulated front velocity as can be seen in figure 9. This velocity depends on the ionization frequency as expected, but also on the diffusion coefficient. Actually the variation of the front velocity is mainly due to the increase of the ionization frequency since the diffusion coefficient does not vary significantly on the range 30 to 40 dBm.

4.2. Steady-state results

The plasma-based microwave power limiter was also measured in steady-state configuration, using the experimental setup of figure 3. The power of the microwave signal at the input of the DUT was swept

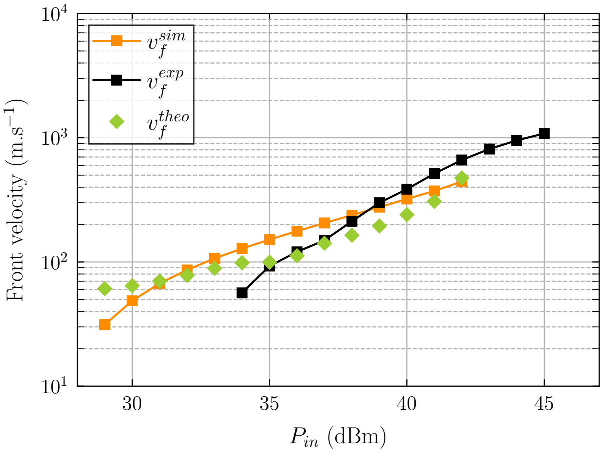

Figure 9. Simulated, measured and theoretical front velocities as a function of the input power P_{in} at 3 GHz with Argon at 10 Torr and $I_{DC} = 3$ mA.

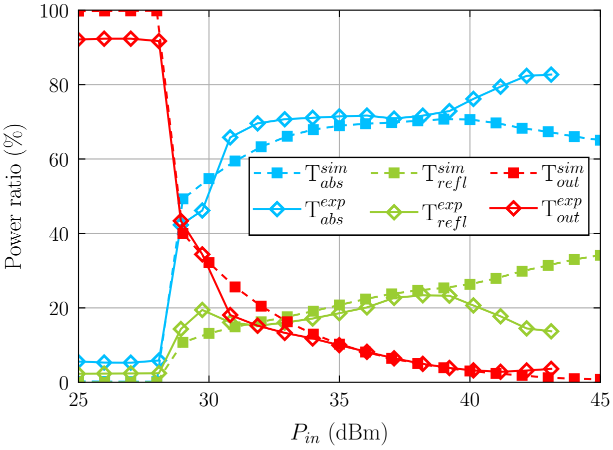

Figure 10. Simulated and measured steady-state power ratios as a function of the input power P_{in} at 3 GHz with Argon at 10 Torr and $I_{DC} = 3$ mA.

from 25 to 45 dBm, and we measured the input, reflected, and output power ratios.

First, it should be noted that without pre-ionization ($I_{DC} = 0$ mA) no microwave power limitation is observed in simulation or measurement with this input microwave power range. The electric field is not large enough for gas breakdown. This result is consistent with [20]. Hereafter, the MHCD is switched on with a DC current I_{DC} equal to 3 mA.

Figure 10 shows the simulated and measured power ratios in steady-state as a function of the input power. We observe the typical response of a mainly absorptive microwave power limiter. Indeed, all the power ratios remain constant when P_{in} is lower than the limiting threshold of 28 dBm. The limiter is in the "off" state. When P_{in} exceeds 28 dBm, microwave breakdown occurs and the output power ratio decreases while the reflected and dissipated power ratios increase. We note that in the "on" state, the decrease of the output power is mainly due to the absorption of the HPM signal by the plasma. It is consistent with other results obtained for wideband plasma-based microwave power limiter [20].

The simulated and measured power ratios in figure 10 show good overall agreement. Slight discrepancies are observed for low input power. They are mainly due to the fact that the model does not take into account the dielectric losses in the substrate and the coaxial to transmission line transitions which are responsible for a slight impedance mismatch in the DUT. Besides, for input power larger than 40 dBm, simulated and measured power ratios slightly diverge. Two hypotheses can explain these discrepancies. First, during measurements, due to a defect in the assembly of the DUT, the plasma tended to penetrate between the upper part of the dielectric spacer and the dielectric substrate of the suspended microstrip. Such behaviour is not possible in simulation. Secondly, considering that the microwave input power is mainly absorbed by the plasma, thermal effects may occur in the discharge for such high P_{in} values that can affect the local pressure of the gas. Such effects are not taken into account by the model, which may also explain the difference between simulated and measured results at high input power.

The steady state numerical solutions for the ion and electron densities and for the electron temperature are presented in figure 11 as a function of position for the three input powers $P_{in} = 30$ dBm, $P_{in} = 35$ dBm and $P_{in} = 40$ dBm. All these profiles have also been averaged over the plasma domain, along the y axis. The plasma density increases with the incident power as well as the length of the plasma column. The maximum values of $\langle n \rangle_y$ are 3.01×10^{18}, 1.26×10^{19}, 3.34×10^{19} and the length of the plasma columns (the end of the plasma columns are represented by the black dashed lines on figure 11) are of 13.8 mm, 22.8 mm, and 33.6 mm, for each incident power respectively. The electron temperature is uniform in the plasma, and is approximately equal to 3.45 eV, whatever the incident power.

The simulated plasma density is higher than the critical density whatever the incident power. The critical density at 3 GHz is of $n_c = 1.12 \times 10^{17}$ m^{-3}. The positions for which $\langle n_e \rangle_y = n_c$ are represented by the black dashed lines for each profile. These positions correspond approximately to the ones where the quasi-neutrality is broken, that is to say, to the end of the plasma columns, where the electron temperatures start to decrease.

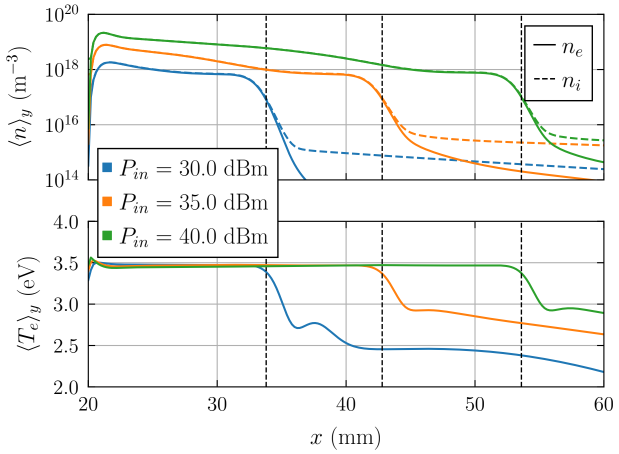

Figure 11. Simulated electron and ions density profiles and electron temperature profile as a function of the position for $P_{in} \in [30.0, 35.0, 40.0]$ dBm at 3 GHz with Argon at 10 Torr.

5. Conclusion

A plasma-based microwave power limiter has been proposed in a suspended microstrip technology. The incident electric field here ignites a plasma discharge in Argon at 10 Torr that absorbs and reflects the microwave power and thus reduces the level of the signal at the output of the device. The use of a MHCD (Micro Hollow Cathod Discharge) allows to drastically decrease the magnitude of the electric field necessary to ensure microwave gas breakdown.

The performances of the limiter have been studied experimentally by measuring the output and absorbed power. These results have also been compared with numerical ones obtained from a self-consistent model that simulates the non linear interaction between the microwave field and the plasma. A simple chemical model have been proposed, that implies four states: neutral argon, effective metastable and resonant states, and one molecular ion. The reaction rates have been calculated with the BOLSIG+ software, with a self-calculated electron energy distribution function.

The simulations have shown a very good agreement with the experimental results, both in steady state and transient regime, for input powers lower than 40 dBm. These simulations allowed us to accurately link the time evolution of the power ratios with the dynamics of the plasma in the DUT. The propagation of an ionization wave from the MHCD source toward the microwave source is observed both numerically and experimentally. In our plasma discharge, the creation of electrons is mainly due to the step-wise ionization from metastable and resonant states. From numerical results, we deduced that the propagation is due to the gap between the positions of the maximum of the source term for the electrons and the maximum of the electron density. A theoretical model has shown that the propagation velocity depends on the diffusion of the electrons at the head of the ionization front, and on the ionization frequency.

These results allow us to use this model to explore possibles improvement of the system. However, for input powers higher than 40 dBm, the experimental and numerical results diverge and the dynamics of the plasma is not well described by the model. Further studies will be conducted in to understand the causes of this phenomenon.

Acknowledgments

The authors would like to thank the Délégation Générale pour l'Armement (DGA), the Agence de l'Innovation de Défense (AID), the Région Occitanie Pyrénées-Méditerranée and the Agence Nationale de la Recherche (ANR-21-ASM1-0002) for their financial support.

References

[1] Zhang J, Zhang D, Fan Y, He J, Ge X, Zhang X, Ju J and Xun T 2020 *Phys. Plasmas* **27**
[2] Backstrom M G and Lovstrand K G 2004 *IEEE Trans. Electromagn. Compat.* **46** 396–403
[3] Bilotta R F 1997 *Microw. J.* **40** 90–96
[4] Shojaei-Asanjan D and Mansour R R 2016 *IEEE Trans. Microw. Theory Tech.* **64** 4473–4481
[5] Booth J C, Rudman D A and Ono R H 2003 *IEEE Trans. Appl. Supercond.* **13** 305–310
[6] Belyaev B A, Govorun I V, Leksikov A A, Serzhantov A M and Leksikov A A 2016 *IEEE Trans. Appl. Supercond.* **26** 1500506
[7] Givernaud J, Crunteanu A, Orlianges J C, Pothier A, Champeaux C, Catherinot A and Blondy P 2010 *IEEE Trans. Microw. Theory Tech.* **58** 2352–2361
[8] Looney J, Conway D and Bahl I 2004 *IEEE Microw. Mag.* **5** 83–86
[9] Yang S S, Kim T Y, Kong D K, Kim S S and Yeom K W 2009 *IEEE Trans. Microw. Theory Tech.* **57** 1447–1460
[10] Yang L, Yang L A, Rong T, Li Y, Jin Z and Hao Y 2019 *IEEE Access* **7** 88275–88281
[11] Zhao J, Chen Q, Zhao G, Chen C and Chen Z 2020 *Sci. Rep.* **10**
[12] Smullin L D and Montgomery C G 1948 *Microwave Duplexers* vol 14 of MIT Radiation Laboratory Series (McGraw-Hill)
[13] Patel S D, Dubrowsky L, Saddow S E, Kaul R and Garver R V 1989 Microstrip plasma limiter *IEEE MTT-S Int. Microw. Symp. Dig.* vol 3 pp 879–882
[14] Cross L W, Almalkawi M J and Devabhaktuni V K 2013 *IEEE Trans. Electromagn. Compat.* **55** 1100–1106
[15] Pascaud R, Pizarro F, Callegari T, Liard L, Pigaglio O and Pascal O 2015 *Electron. Lett.* **51** 1090–1092
[16] Semnani A, Macheret S O and Peroulis D 2016 *IEEE Trans. Plasma Sci.* **44** 3271–3280
[17] Parsons S, Gregório J and Hopwood J 2017 *Plasma Sources Sci. Technol.* **26** 055002
[18] Simon A, Pascaud R, Callegari T, Liard L, Pascal O and Pigaglio O 2017 Static and dynamic control of limiting threshold in plasma-based microstrip microwave power limiter *IEEE MTT-S Int. Microw. Symp. Dig.*

[19] Parsons S G and Hopwood J 2017 *IEEE Electron Device Lett.* **38** 1602–1605

[20] Simon A, Pascaud R, Callegari T, Liard L and Pascal O 2018 *IEEE Trans. Plasma Sci.* **46** 2512–2520

[21] Kim H and Hopwood J 2020 *J. Appl. Phys.* **128**

[22] Missen Z V, Semnani A and Peroulis D 2020 *IEEE Access* **8** 173103–173111

[23] Bandel H W and MacDonald A D 1969 *J. Appl. Phys.* **40** 4390–4394

[24] Gregório J, Parsons S and Hopwood J 2017 *Plasma Sources Sci. Technol.* **26**

[25] Schoenbach K H, El-Habachi A, Shi W and Ciocca M 1997 *Plasma Sources Sci. Technol.* **6** 468–477

[26] Boeuf J P, Pitchford L C and Schoenbach K H 2005 *Appl. Phys. Lett.* **86** 071501

[27] Hagelaar G J M, Makasheva K, Garrigues L and Boeuf J P 2009 *J. Phys. D: Appl. Phys.* **42**

[28] Collin R E 2001 *Foundations for Microwave Engineering, Second Edition* (Wiley-IEEE Press)

[29] Taflove A and Hagness S C 2005 *Computational Electrodynamics: The Finite-Difference Time-Domain Method, Third Edition* (Artech House)

[30] Morgan database, www.lxcat.net/Morgan, retrieved on July 15, 2020

[31] Deutsch H, Becker K, Grum-Grzhimailo A N, Bartschat K, Summerse H, Probst M, Matt-Leubner S and Märk T D 2004 *Int. J. Mass Spectrom.* **233** 39–43

[32] Deutsch H, Becker K, Matt S and Märk T D 2000 *Int. J. Mass Spectrom.* **197** 37–69

[33] Deutsch H, Becker K, Matt S and Märk T D 1999 *J. Phys. B: At. Mol. Opt. Phys.* **32** 4249–4259

[34] BSR database (Quantum-mechanical calculations by O. Zatsarinny and K. Bartschat), www.lxcat.net/BSR, retrieved on July 15, 2020

[35] Holstein T 1947 *Phys. Rev.* **72** 1212–1233

[36] Holstein T 1951 *Phys. Rev.* **83** 1159–1168

[37] NIST database, http://www.nist.gov/index.html

[38] Ferreira C M and Ricard A 1983 *J. Appl. Phys.* **54** 2261–2271

[39] Lam S, Zheng C E, Lo D, Dem'yanov A and Napartovich A 2000 *J. Phys. D: Appl. Phys.* **33** 242

[40] Mehr F J and Biondi M 1968 *Phys. Rev.* **176** 322–326

[41] Hagelaar G J M and Pitchford L C 2005 *Plasma Sources Sci. Technol.* **14** 722–733

[42] Ebert U and van Saarloos W 2000 *Physica D* **146** 1–99

[43] Boeuf J P, Chaudhury B and Zhu G Q 2010 *Phys. Rev. Lett.* **104** 015002